Progress In Electromagnetics Research, Vol. 122, 519–535, 2012

SUSPENDED SUBSTRATE STRIPLINE BANDPASS FILTERS WITH SOURCE-LOAD COUPLING STRUCTURE USING LUMPED AND FULL-WAVE MIXED APPROACH

M.-H. Ho* and P.-F. Chen

Graduate Institute of Communications Engineering, National Changhua University of Education, #2, Shih-Da Road, Changhua City 50074, Taiwan

Abstract—This paper presents the design of two suspended substrate stripline (SSS) bandpass filters (BPFs), both with a source-load coupling structure embedded to create a transmission zero (TZ) near each side of the passband edges. For the first BPF, the physical circuit layout is proposed first and followed by the establishment of an equivalent LC circuit. The optimization of element values of the LC circuit using a circuit-level simulator leads to quick adjustment of the structural parameters of the physical circuit layout with the aid of a full-wave simulator. For the second BPF, the ingenious equivalent LC circuit modified from that of the first one is proposed for bandwidth enhancement, which is achieved by exciting two extra loaded resonances in the passband. With the element values of the LC circuit optimized, proper reshaping the physical circuit layout from that of the first BPF is easily accomplished. The presented lumped and full-wave mixed approach is very efficient in that the circuit-level simulator is used to the largest extent and the time-consuming full-wave simulator is employed only at the later stage of the design. Experiments are conducted to verify the design of the two SSS BPFs and agreements are observed between the measured and simulated data.

1. INTRODUCTION

The suspended substrate stripline (SSS), frequently called suspended stripline for short, is a printed circuit technology that can be used for both narrowband and broadband filters in low-pass, high-pass,

Received 25 October 2011, Accepted 30 November 2011, Scheduled 8 December 2011
* Corresponding author: Min-Hua Ho (ho@cc.ncue.edu.tw).

band-pass, bandstop, and multiplexer forms. It was first proposed by Rooney and Underkoefler [1] in 1978. Recently, Fardis and Khosravi [2] extended the scope of SSS to a periodical SSS structure, analyzing its field propagation. Because of their wider range of realizable characteristic impedances and higher reachable quality factors than those of many other planar structures, such as microstrips, striplines, slotlines, and coplanar waveguides, SSS structures have held the edge in filter design. In an SSS configuration, the substrate suspended in air is enclosed by a metal channel of rectangular cross section, and hence most of the electromagnetic field is distributed in air. This causes the SSS structure to have a lower loss, a higher quality factor, and sharper band edges. In addition, the SSS structure is more flexible to design in that the circuit patterns are allowed to be deployed on both sides of the substrate. This is because the metal ground printed on the substrate can be removed, with the metal housing serving as the ground instead. Furthermore, the metal housing protects the circuit against environmental electromagnetic interference and conversely prevents the circuit from radiating into the exterior space. In building a filter, the housing may be fitted with a variety of RF connectors or be equipped with 50-Ω feed-throughs for direct connection to MICs.

In the past, filtering circuits designed using SSS structures were proposed by Rhodes and Mobbs [3, 4], who constructed filters and diplexers in various forms. In [5, 6], Belyaev et al. miniaturized SSS BPFs with high selectivity performance. Similar to SSS structure, a filter with a coaxial tube housing the suspended resonators was reported in [7]. Menzel et al. [8–11] used a quasi-lumped approach to design some SSS filters and diplexers. In their works, coupled SSS resonators of various shapes were adopted in filter design. In their quasi-lumped approach, a few lumped inductive and capacitive elements were used to establish an equivalent LC circuit, from which the resonant characteristics of the coupled SSS resonators were studied. However, the equivalent circuit of an entire SSS filter with multiple resonators was never explored for analysis. Hence, full-wave simulations were unavoidably needed to calculate the SSS filter's frequency responses and to verify the design. Sometimes the usage of full-wave simulations is extensive, resulting in an inefficient design process.

In the past, lumped-element circuit models were presented mainly for comprehension purpose, not suitable for the circuit's physical layout design [12–14]. The circuit layout as well as the structural dimensions was still determined by full-wave simulations, requiring a considerable computational resource. In fact, full-wave simulations can be carried out only at a later stage of the design process if the quasi-lumped

approach can be extensively employed throughout the entire design process. For given filter specifications, a circuit layout configuration can be proposed first, and subsequently a corresponding meaningful LC circuit model (or alternatively called quasi-lumped circuit model) representing the complete filter structure can be established. The element values of the equivalent LC circuit can then be optimized using a circuit-level simulator. Once these LC element values are obtained, structural dimensions of the circuit layout can be adjusted accordingly since there is a meaningful correspondence between each lumped circuit element and some specific part of the circuit layout. It is only at this stage that a full-wave simulator is required, and hence the burden of extensive full-wave simulations might be alleviated. It is well understood that optimizing the element values of the lumped circuit using a circuit-level simulator is much more efficient than adjusting the structural dimensions of the circuit layout using a full-wave simulator. Alternatively, since quasi-lumped elements can be associated with or mapped to some particular physical layout in SSS structures [10, 15], one can also propose a quasi-lumped circuit first and then optimize its element values using a circuit-level simulator. Next, explore possible physical circuit layout that corresponds to the just established quasi-lumped circuit and then adjust its structural dimensions using a full-wave simulator. In short, as an auxiliary yet very efficient tool, a circuit-level simulator can be used to the largest extent in designing an SSS filter, leaving the full-wave simulator to be employed as late as possible in the design process and thus minimizing relatively inefficient full-wave simulations.

In this paper, two BPFs are presented, one being of narrower band and the other of wider band. For convenience, the former is called BPF A, and the latter BPF B. The circuit pattern of BPF A (BPF B) is printed on a 10-mil-thick and 5-mm-wide (7-mm-wide) RT/Duroid 5880 substrate with dielectric constant 2.2 and loss tangent 0.0009. Each printed substrate horizontally lies inside a metal enclosure having an interior 5- or 7-mm-wide and 4.254-mm-high rectangular cross section, with 2-mm-thick air zones above and below the substrate. Source-load coupling for enhancing signal selectivity of the passband is incorporated in both BPFs to demonstrate the flexibility of the design. Note that the source-load coupling commonly seen in filters of many forms using other planar structures [16–19] is perhaps for the first time applied to SSS structures, to the best of the authors' knowledge. Although a cross coupling structure similar to the source-load one was reported in [6] in the SSS filter design, the adjustment of transmission zeros in their design rather relies mainly on the cancelation of inductive and capacitive couplings within its dual-mode resonator, whereas the

locations of transmission zeros in our proposed BPFs are dominated and can be well controlled by the source-load coupling. For the purpose of establishing the source-load coupling, the SSS resonator is printed on the side opposite to the feed-lines extended from the signal lines of the SMA connectors, thus allowing the two feed-lines to be brought closer to establish the source-load coupling without increasing the circuit size. For BPF A, a circuit layout is proposed first and is followed by the establishment of the equivalent quasi-lumped circuit. In particular, two narrow strips in the middle of a half-wavelength SSS resonator are short-circuited to the bilateral walls of the housing, a configuration that can also be found in [20]. These grounded strips effectively transform the SSS resonator from a single-mode resonator to a dual-mode one. It is found that from even- and odd-mode analyses of the equivalent quasi-lumped circuit, one can accurately predict the two dips in the reflection-coefficient curve and the two TZs near the two passband edges. For BPF B, the design starts with establishing a quasi-lumped circuit and is followed by exploring a possible physical layout. The quasi-lumped circuit is actually obtained through cleverly modifying the one for BPF A, of course, with the aid of a circuit-level simulator. The augmentation of the passband is mainly due to the excitation of two additional resonant modes in the structure. From the modification of the quasi-lumped circuit, a possible physical circuit layout can be easily developed. Experiments are conducted to verify the design of these two BPFs and agreements are observed between the measured and the simulated data.

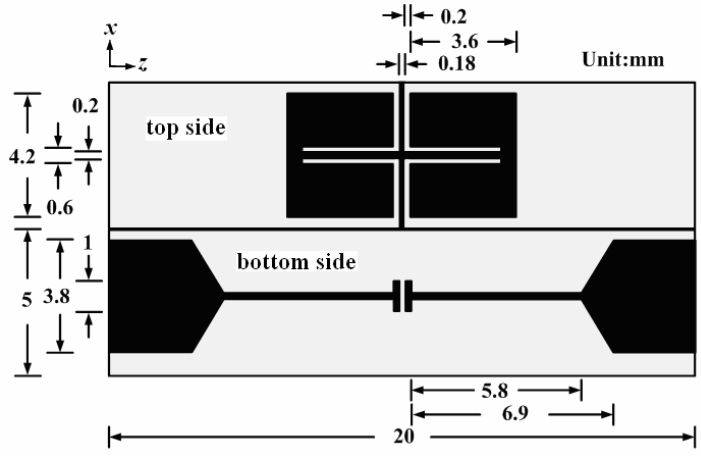

Figure 1. The proposed circuit layouts on the two sides of the substrate of BPF A.

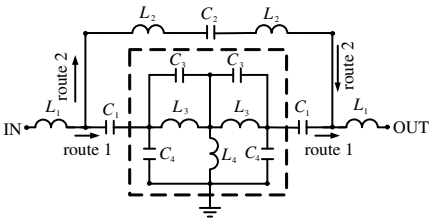

Figure 2. The developed LC circuit model for BPF A in Figure 1.

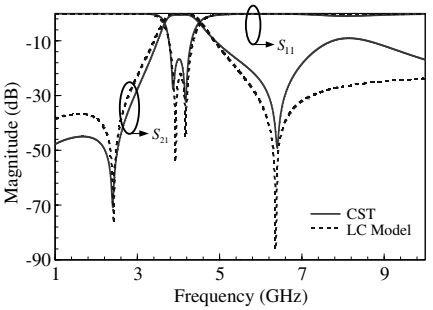

Figure 3. Simulated frequency response of the LC circuit in Figure 2 and CST-simulated data.

2. DESIGN OF BPF A

Figure 1 shows the printed circuit patterns on the top and bottom sides of the substrate of BPF A, in which two signal paths exist between the input and output ports. Along the first path (referred to as route 1), signals entering the input feedline on the bottom side couple to the resonator on the top side first and then couple to the output feedline. Along the second path (called route 2), signals entering the input feedline directly couple to the output feedline through the end-coupling gap in between. The cross coupling owing to signals passing through these two routes may result in TZs by the passband edges. Shown in Figure 2 is an equivalent quasi-lumped circuit with routes 1 and 2 indicated. In this LC circuit, the part of the circuit enclosed by a dashed rectangular box represents the resonator on the top side of the substrate and the elements along route 2 denote the source-load coupling structure. The inductances L_1 correspond to the narrow feedlines not shaded on top by the resonant SSS patch, while the inductances L_2 pertain to the rest of the feedlines. The capacitances C_1 denote the couplings between the SSS patch and the feedlines, while the capacitance C_2 represents the direct coupling between the input and output feedlines. The inductances L_3 correspond to the z-directed narrow strip of the SSS resonator that is bisected by the grounded x-directed narrow strip, whose effect on the resonator is represented by the grounded inductances L_4. The capacitances C_3 denote the coupling between the four x-directed inner edges and the center of the resonator, while the capacitances C_4 characterize the couplings between the z-directed outer edges of the resonator and the bilateral walls of the metal housing.

Once the LC circuit model is created, the circuit can be thoroughly investigated by using a circuit-level simulator. Among many commercial circuit-level simulators, the circuit-simulation function of the Agilent ADS [21] is adopted in this paper for that purpose. With the aid of the circuit-level simulator, the values of the lumped elements can be optimized so that the frequency response of the equivalent LC circuit can approach the given filter specifications, a procedure that has been exercised in [15]. Because of the correspondence between the physical layout in Figure 1 and the lumped elements in Figure 2, the optimized LC values will suggest to us how to adjust the physical layout of the BPF circuit using a full-wave simulator (the simulator CST [22] is adopted in this paper). For example, for a larger L_4, the x-directed grounded strip may be modified to have a narrower width; for a smaller C_2, the gap between the input and output feedlines may be enlarged. Changes in the remaining LC parameters are also associated with some other appropriate modifications in the physical layout. For conciseness, the appropriate modification will not be discussed one by one. For a 3-dB passband of 3.7–4.4 GHz, the structural dimensions of the proposed prototype BPF in Figure 1 are obtained with only a few iterations of CST simulation and are indicated in the figure. The corresponding LC values of Figure 2 are $L_1 = 0.0324\,\text{nH}$, $L_2 = 0.097\,\text{nH}$, $L_3 = 1.26\,\text{nH}$, $L_4 = 0.25\,\text{nH}$, $C_1 = 0.403\,\text{pF}$, $C_2 = 0.0207\,\text{pF}$, $C_3 = 0.016\,\text{pF}$, and $C_4 = 0.71\,\text{pF}$. Simulated S-parameters for Figures 1 and 2 are presented in Figure 3 for comparison. They agree reasonably well with each other except for the frequency range beyond the higher TZ. This is of no surprise since at high frequencies simple quasi-lumped circuit elements are not expected to fully take into account all the complicated mutually coupling effects of the physical circuit layout.

The agreement in frequency response for the circuits in Figures 1 and 2 suggests that more insight of the circuit behavior can be investigated by solely examining the equivalent LC circuit. Since the circuit is symmetric with respect to the middle point between the input and output ports, the two-port scattering parameters can be derived from the reflection coefficients of two equivalent one-port half-circuits, one for the even mode and the other for the odd mode. The equivalent even- and odd-mode one-port half-circuits, shown in Figures 4(a) and 4(b), respectively, can be obtained by opening and grounding the complete LC circuit at its plane of symmetry. To this end, let us first examine how the coupling capacitance C_1 affects the resonant frequencies of the unloaded resonator. For that purpose, the unloaded resonator circuit and the coupling capacitance C_1 are redrawn in Figure 5. In this figure, C_1 has been replaced by an admittance inverter

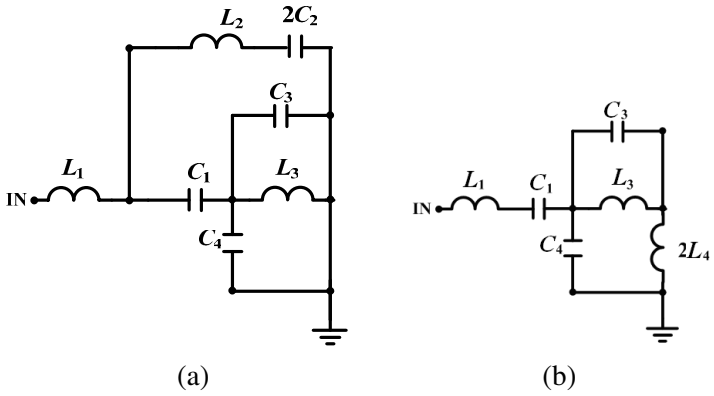

Figure 4. The equivalent one-port half-circuits of the LC circuit in Figure 2 for the (a) odd and (b) even modes.

of characteristic admittance $J = \omega C_1$ shunted at both sides with C_1. The unloaded resonator circuit denoted by the rectangular box may be the equivalent even- or odd-mode half-circuit of the unloaded resonator, depending on whether even- or odd-mode resonant behavior is being investigated. The unloaded resonant frequency is the frequency such that $Y_a = 0$. With the presence of the coupling capacitance, the resonant frequency observed may be quite different from that of the unloaded resonator. For convenience, the new frequency of interest at which $Y_b = 0$ can be called the coupled resonant frequency. Obviously, the shunted C_1 in parallel with the unloaded parallel resonant circuit will cause the coupled resonant frequency to be lower than the unloaded one. Because the inverter can transform a parallel resonance into a series resonance, the coupled resonant frequency is also the frequency at which $Z_c = Z_d = 0$. The phenomenon that the resonant frequency detected through a series capacitive coupling is lower than the inherent unloaded resonant frequency of a parallel resonant circuit has also been derived in a slightly different manner in [23].

With the LC values given previously, the unloaded resonant frequencies are found to be 5.26 and 4.47 GHz (5.32 and 4.56 GHz from CST simulation) for the odd- and even-mode resonances, whereas the coupled resonant frequencies of the circuit in Figure 5 are lowered to 4.21 and 3.58 GHz, respectively. Note that these coupled resonant frequencies can be easily identified as the frequencies at which the reflection phase (i.e., the phase of the reflection coefficient) of the circuit in Figure 5 is 180° since at these frequencies $Z_d = 0$. For the equivalent one-port half-circuits in Figure 4, the resonant frequency

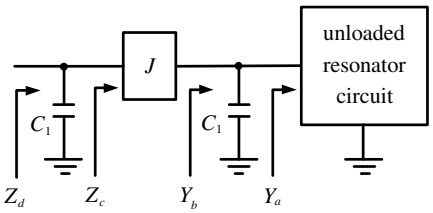

Figure 5. The LC circuit of a capacitance-coupled resonator.

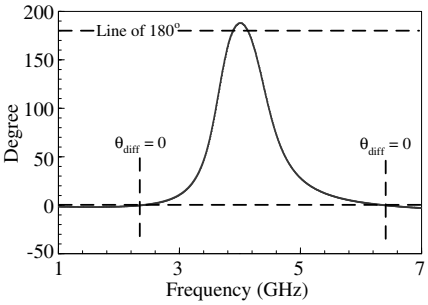

Figure 6. Difference in reflection phase between the circuits in Figures 4(a) and 4(b).

can also be defined as the one at which $\theta_{\Gamma,\text{even}} = 180°$ or $\theta_{\Gamma,\text{odd}} = 180°$, where $\theta_{\Gamma,\text{even}}$ and $\theta_{\Gamma,\text{odd}}$ are the phases of the reflection coefficients Γ_{even} and Γ_{odd}, respectively. For differentiation, we refer to these frequencies as the loaded resonant frequencies. Because the values of L_1, L_2, and C_2 are relatively small as compared with those of the unloaded resonator circuit and C_1, the loaded resonant frequencies are very close to the coupled resonant frequencies. They are 4.18 and 3.59 GHz, respectively, for the circuits in Figures 4(a) and 4(b). For validation, CST was also adopted to compute the loaded resonant frequencies of the circuit in Figure 1 with the plane of symmetry replaced with an electric and a magnetic wall for the odd- and even-mode operations, respectively. The CST-simulated loaded resonant frequencies of 4.13 and 3.586 GHz are very close to those obtained from the circuit-level simulation, thus proving the validity of the quasi-lumped circuit model.

Note that $S_{11} = (\Gamma_{\text{even}} + \Gamma_{\text{odd}})/2$ and $S_{21} = (\Gamma_{\text{even}} - \Gamma_{\text{odd}})/2$ hold between the two-port circuit and the two one-port half-circuits [24]. Since these circuit models are lossless, it is of no doubt that $|\Gamma_{\text{even}}| = |\Gamma_{\text{odd}}| = 1$ and the reflection zeros of the two-port circuit occur when the reflection-phase difference, defined by $\theta_{\text{diff}} = \theta_{\Gamma,\text{even}} - \theta_{\Gamma,\text{odd}}$, is 180°. On the other hand, the TZs should occur when $\theta_{\text{diff}} = 0$. Figure 6 shows θ_{diff} as a function of frequency, from which $\theta_{\text{diff}} = 180°$ occurs at 3.88 and 4.18 GHz and $\theta_{\text{diff}} = 0$ occurs at 2.42 and 6.4 GHz. As can be seen from Figure 3, these circuit-level-simulated reflection and TZs are indeed very close to the CST-simulated reflection zeros of 3.84 and 4.2 GHz and TZs of 2.42 and 6.42 GHz, a result further proving the validity of the quasi-lumped circuit model.

Note that the TZs can be attributed to the cancelation of the signals passing through two different routes, i.e., route 1 serving as

the main path and route 2 behaving as the cross-coupling path. This cross-coupling path is established by connecting the input and output feedlines to two short, yet tightly coupled parallel line sections. This source-load coupling, appearing in an SSS structure perhaps for the first time, enables the filter to implant two TZs by the pass-band edges for enhancing signal selectivity. To demonstrate the cross coupling effect, the transmission responses $|S_{21}|$ for route 1 only (with C_2 set to zero), route 2 only (with C_1 set to zero), and the complete circuit are presented in Figure 7. Also shown in this figure is the difference between the phase of $|S_{21}|$ for route 1 and that for route 2. At the TZs of 2.42 and 6.4 GHz, $|S_{21}|$ for route 1 is about the same as that for route 2; the phase difference is close to an odd multiple of 180°. Note that the demonstration here is only heuristic in nature and is by no means rigorous. If at a TZ a signal entering the complete circuit is equally allotted to the two paths, $|S_{21}|$ for route 1 must be exactly the same as that for route 2; and the phase difference must be exactly an odd multiple of 180°.

It can be deduced from Figure 7 that a stronger source-load coupling (i.e., a larger C_2 in the circuit) will result in a higher $|S_{21}|$ curve for route 2. This in turn causes a closer spacing between the two intercept points made by the two $|S_{21}|$ curves, one for route 1 and the other for route 2, thus making the TZs approach more toward the pass-band edges. Shown in Figure 8 are the frequency responses for several different coupling strengths (denoted by C_2). The one without any source-load coupling (denoted by $C_2 = 0$) does not have a TZ in the displayed frequency range. As just deduced from Figure 7, it appears that a stronger source-load coupling drives the TZs closer to the pass-band edges, resulting in a better signal selectivity and sharper roll-off of

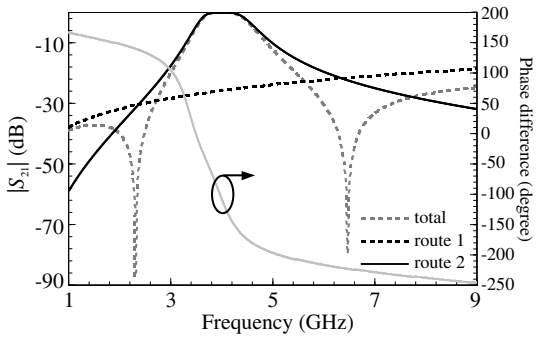

Figure 7. Simulated transmission response of the LC circuit in Figure 2.

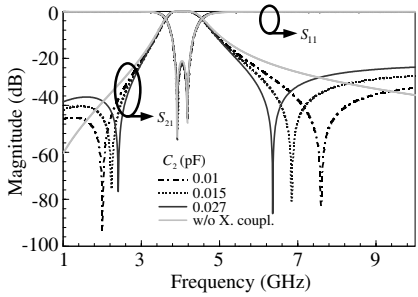

Figure 8. Simulated frequency responses of the LC circuit in Figure 2 for several different source-load coupling strengths.

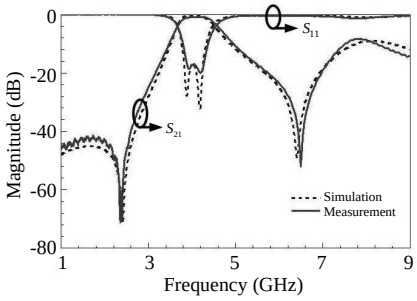

Figure 9. The measured and CST-simulated frequency responses of BPF A.

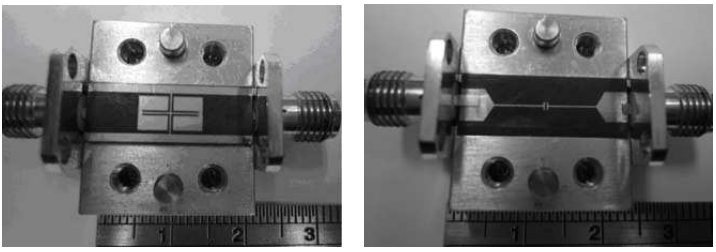

Figure 10. The photos of BPF A with the (a) top and (b) bottom sides of the printed substrate facing up.

the pass-band edges. However, this trend cannot go unboundedly. The value of $C_2 = 0.0207\,\text{pF}$ is the upper limit for the source-load coupling without deteriorating the pass-band performance of this circuit.

Once the LC element values have been optimized by using the circuit-level simulator, the dimensions of the physical layout can be subsequently adjusted. Since the dimensions are adjusted according to the obtained LC values, not simply by trials-and-errors, the fine-tune process can be ended in just a few iterations of CST simulations, thus rendering a very efficient design process. The resultant dimensions of the physical layout are shown in Figure 1, and the measured and CST-simulated frequency responses of the designed BPF A are presented in Figure 9. The measured data agree quite well with the simulated ones. The measured (simulated) 3-dB pass-band has a bandwidth of 0.81 GHz (0.79 GHz) and a center frequency of 4.1 GHz (4.09 GHz).

The measured (simulated) maximum in-band insertion loss is 0.7 dB (0.53 dB). The measured transmissions zeros due to the cross-coupling effect are at the frequencies of 2.41 GHz and 6.5 GHz, approaching the simulated ones of 2.42 GHz and 6.42 GHz, respectively. The designed reflection zeros located at 3.84 GHz and 4.2 GHz are very close to the ones measured at 3.92 GHz and 4.28 GHz, respectively. Figures 10(a) and 10(b), respectively, show the photographs of the BPF with (a) the top and (b) the bottom sides of the printed substrate facing up and supported by one half of the metal housing.

3. DESIGN OF BPF B

In BPF A, the feedline directly couples electromagnetic energy to the resonator through the capacitance C_1 to simultaneously generate both odd- and even-mode coupled resonances. In this section, we aim at designing the other BPF (i.e., BPF B) whose structure is modified from that of BPF A and whose bandwidth is much wider than that of BPF A. For that purpose, the number of coupled resonances in the passband should be increased. To accomplish that goal, an alternative coupling route in parallel with the original one is needed to produce two extra coupled resonances whose resonant frequencies should be different from those of the existing ones (i.e., the coupled resonances associated with C_1). To distinguish the resulting two additional resonances from the original ones, the alternative coupling requires its coupling strength much different from that of the original coupling route. Upon a further survey of the equivalent LC circuit model of BPF A in Figure 2, we can regard the original coupling route that provides coupling between the feedline and the overlapped resonator via C_1 as a direct one. This suggests to us that the alternative coupling route between the feedline and the resonator may be chosen to be indirect. The most convenient solution might be the one which diverts signals from the feedline to the resonator via an object in between. In observing the circuit layout of BPF A in Figure 1, the indirect path can be formed by placing an extra patch by each side of the resonator to relay signals. Thus, the created route is collateral to the original one, exciting extra coupled resonances. From a few tries using the ADS circuit simulator, the capacitance C_4 originally connected to the ground is now parallel to C_1 and connects to a shunt circuit block placed before C_1 in the LC circuit model as shown in Figure 11. The shunt circuit block represents the added patch. Upon performing these modifications, the resulting wide-band LC circuit model (Figure 11) exhibits two pairs of bundled odd- and even-mode resonances caused by two coupling routes. A few minor changes also are needed in building the wide-band LC circuit

model, including a decreased L_3, an increased L_4, and a much larger C_4 as compared with C_1.

With the elements of the LC circuit optimized to be $L_{1a} = 1.075\,\text{nH}$, $L_{1b} = 2.215\,\text{nH}$, $L_2 = 0.265\,\text{nH}$, $L_3 = 0.57\,\text{nH}$, $L_4 = 0.4\,\text{nH}$, $L_{5a} = 0.411\,\text{nH}$, $L_{5b} = 0.01\,\text{nH}$, $C_1 = 0.365\,\text{pF}$, $C_2 = 0.01\,\text{pF}$, $C_3 = 0.04\,\text{pF}$, $C_4 = 1.15\,\text{pF}$, and $C_5 = 0.074\,\text{pF}$, the loaded odd-mode (even-mode) resonant frequencies occur at 4.06 and 6.76 GHz (3.15 and 5.78 GHz), at which $\Gamma_{\text{odd}} = -1$ or $\theta_{\Gamma,\text{odd}} = 180^\circ$ ($\Gamma_{\text{even}} = -1$ or $\theta_{\Gamma,\text{even}} = 180^\circ$), as can be seen in Figure 12. Similar to those defined for the equivalent half-circuits in Figure 4, here Γ_{odd} ($\theta_{\Gamma,\text{odd}}$) and Γ_{even} ($\theta_{\Gamma,\text{even}}$), respectively, are the reflection coefficients (phases)

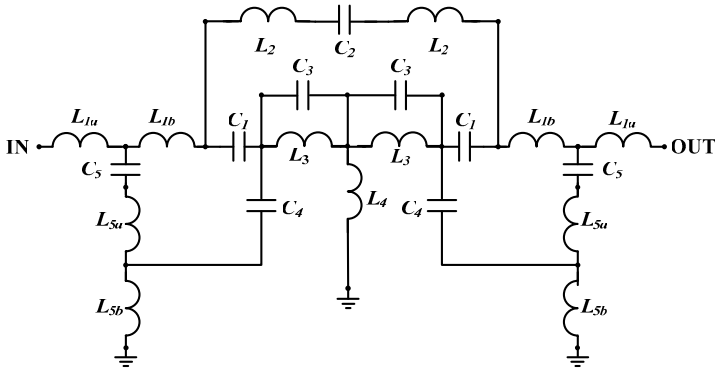

Figure 11. The LC circuit model for BPF B.

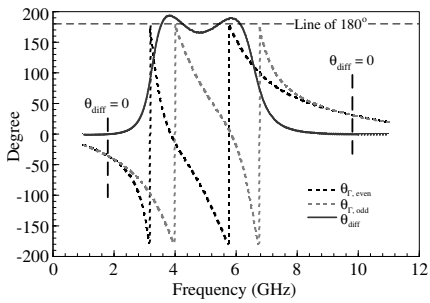

Figure 12. The plots of $\theta_{\Gamma,\text{odd}}$, $\theta_{\Gamma,\text{even}}$, and θ_{diff} for the equivalent half-circuits of the full LC circuit in Figure 11.

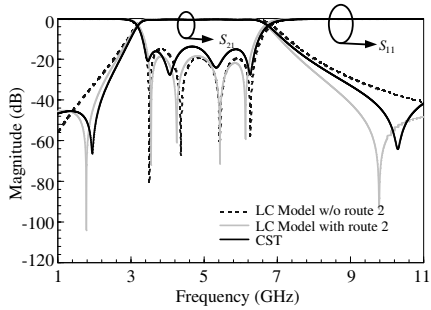

Figure 13. Simulated frequency responses of the LC circuit in Figure 11 with and without the cross-coupling effect and CST-simulated data.

of the equivalent odd- and even-mode half-circuits of the LC circuit in Figure 11. In addition, the reflection zeros at which the condition of $\theta_{\text{diff}} = 180^\circ$ (or equivalently, $\Gamma_{\text{even}} = -\Gamma_{\text{odd}}$) is met at 3.55, 4.24, 5.42, and 6.13 GHz (see Figure 12), which are exactly the frequency locations of the four in-band dips of the grey solid S_{11} curve in Figure 13. Outside the passband, the TZs occur at 1.79 and 9.8 GHz because the condition of $\theta_{\text{diff}} = 0$ (or equivalently, $\Gamma_{\text{even}} = \Gamma_{\text{odd}}$) is met there (see Figure 12). As in BPF B, the locations of TZs are greatly affected by the source-load coupling strength that is represented by C_2. Without the source-load coupling ($C_2 = 0$), there is no TZ in the displayed frequency range of Figure 13. When C_2 is doubled to 0.02 pF, the two TZs are moved closer to the passband edges, located at 2.1 and 8.1 GHz, but with the bandwidth slightly decreased by about 0.3 GHz (not shown here for conciseness).

The physical circuit layout of BPF B under design can be reshaped from that of BPF A to reflect the modifications in the LC circuit model. First, the circuit layout mapped from the decreased L_3 is a shortened z-directed strip in the middle of the resonator; a narrowed x-directed grounded strip corresponds to the increased L_4. Next, C_4 in the alternative coupling route is accomplished by introducing a gap between the added patch and the resonator. As stated above, C_4 ought to be much larger than C_1 for achieving a much wider

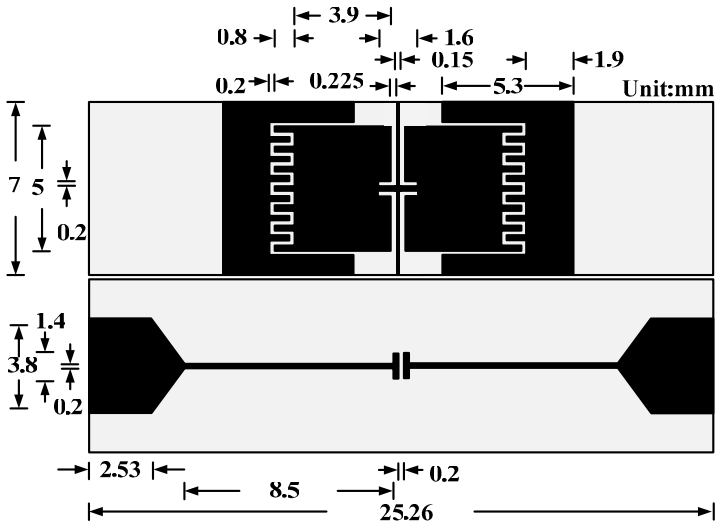

Figure 14. The circuit layouts on two sides of the substrate of BPF B.

passband. A large C_4 can be obtained by replacing the straight gap with an interdigital one, which also prevents an impractically small gap. The shunt circuit consisting of C_5, L_{5a} and L_{5b} in Figure 11 can be realized by an added patch with its two z-directed edges short-circuited to the bilateral walls. At the last stage, the circuit layout is fine tuned by CST simulations to obtain the circuit pattern with its optimized structural dimensions indicated in Figure 14. The CST-simulated frequency response of the BPF in Figure 14 is also shown in Figure 13 for comparison with that of the equivalent circuit in Figure 11. The agreement is reasonable except for the higher-frequency region, in which accurate mutually inductive and capacitive coupling cannot be accounted for in such a simplified equivalent circuit model. The four CST-simulated S_{11} dips are not as deep as those of the LC circuit, for the former are obtained for the physical BPF that is lossy in nature and the latter for the equivalent LC circuit that is free of loss. Although a wider spread of S_{11} dips in the passband will lead to a larger bandwidth, the distribution should be dense enough to avoid deteriorating the passband flatness. In addition, these S_{11} dips should be evenly distributed to result in the smallest transmission ripples.

Figure 15 shows the measured and CST-simulated frequency responses of BPF B. The measurement agrees reasonably well with the simulation. The measured (simulated) data show a passband of 3.1–7 (3.1–6.7) GHz with a fractional bandwidth of 77% (73.5%) and with a maximum in-band insertion loss of 0.85 dB (0.48 dB). The achieved fractional bandwidth is much larger than that of BPF A, for which the measured one is only 19.7%. The photographs of the fabricated BPF are provided in Figure 16.

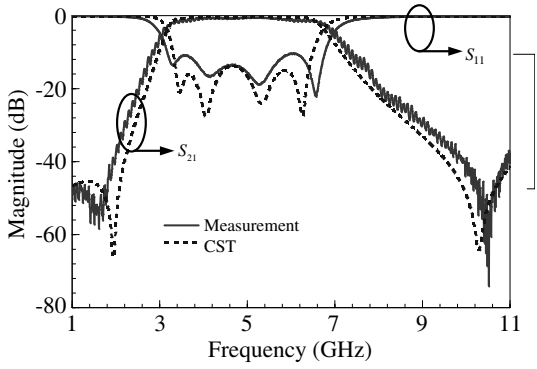

Figure 15. The measured and simulated frequency responses for BPF B.

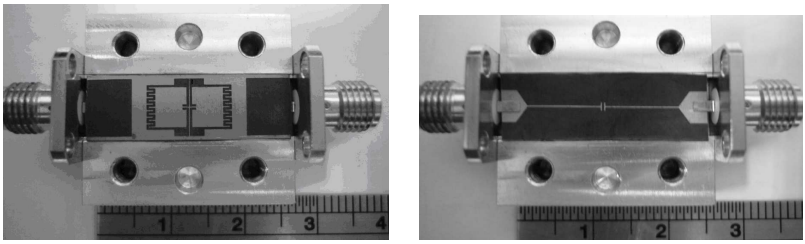

(a) (b)

Figure 16. The photos of BPF B with the (a) top and (b) bottom sides of the printed substrate facing up.

4. CONCLUSIONS

In this paper, a lumped and full-wave mixed approach has been applied for designing two SSS BPFs. In this approach, the equivalent LC circuit can be established after or before the physical circuit layout of the BPF under design is proposed. With the circuit-level simulation function of ADS extensively used to optimize the element values of the equivalent LC circuit of the BPF, the corresponding physical layout, which if not yet available can be mapped from the LC circuit, was subsequently fine tuned with the aid of the full-wave simulator CST. The circuit-level-simulated and CST-simulated data agree reasonably well with each other, validating the mixed approach. Since the circuit-level simulator was extensively applied in the design and the relatively time-consuming full-wave simulation was carried out only at the later stage of the design, the mixed approach appears much more efficient than that using only the full-wave simulator throughout the entire design process. For both BPFs, a source-load coupling is cleverly embedded in the filter to create the cross-coupling effect, resulting in two TZs by the passband edges for enhancing the signal selectivity. These zeros are dominated by the source-load coupling strength, which can be easily realized and controlled. For the fabricated BPFs, the measurement agrees very well with the CST simulation.

ACKNOWLEDGMENT

This work was supported by the National Science Council of the Republic of China (in Taiwan) under Grant NSC 97-2221-E-018-004-MY2.

REFERENCES

1. Rooney, J. P. and L. M. Underkoefler, "Printed circuit integration of microwave filters," *Microwave J.*, Vol. 21, 68–73, 1978.
2. Fardis, M. and R. Khosravi, "Analysis of periodically loaded suspended substrate structures in millimeter wave," *Progress In Electromagnetics Research B*, Vol. 3, 143–156, 2008.
3. Mobbs, C. I. and J. D. Rhodes, "A generalized Chebyshev suspended substrate stripline bandpass filter," *IEEE Trans. Microwave Theory Tech.*, Vol. 35, No. 5, 397–402, 1983.
4. Rhodes, J. D., "Suspended substrate filters and multiplexers," *Proc. 16th European Microwave Conference*, 8–18, 1986.
5. Belyaev, B. A., A. A. Leksikov, A. M. Serzhantov, and V. V. Tyurnev, "Miniature suspended-substrate bandpass filter," *Progress In Electromagnetics Research C*, Vol. 15, 219–231, 2010.
6. Belyaev, B. A., A. A. Leksikov, A. M. Serzhantov, and V. V. Tyurnev, "Highly selective suspended stripline dual-mode filter," *Progress In Electromagnetics Research Letters*, Vol. 25, 57–66, 2011.
7. Jaimes-Vera, A., I. Llamas-Garro, and A. Corona-Chavez, "Coaxial narrowband filters using a versatile suspended resonator," *Progress In Electromagnetics Research*, Vol. 115, 79–94, 2011.
8. Schwab, W., F. Bögelsack, and W. Menzel, "Multilayer suspended stripline and coplanar line filters," *IEEE Trans. Microwave Theory Tech.*, Vol. 46, No. 7, 1403–1407, 1994.
9. Menzel, W., "A novel miniature suspended stripline filter," *European Microwave Conf.*, 1047–1050, 2003.
10. Menzel, W. and A. Balalem, "Quasi-lumped suspended stripline filters and diplexers," *IEEE Trans. Microwave Theory Tech.*, Vol. 53, No. 10, 3230–3237, 2005.
11. Menzel, W., M. S. Rahman Tito, and L. Zhu, "Low-loss ultra-wideband (UWB) filters using suspended stripline," *Asia-Pacific Microwave Conf., (APMC)*, 2148–2151, 2005.
12. Oraizi, H. and M. S. Esfahlan, "Optimum design of lumped filters incorporating impedance matching by the method of least squares," *Progress In Electromagnetics Research*, Vol. 100, 83–103, 2010.
13. Liao, X.-J., M.-H. Ho, W.-H. Hsu, W.-Q. Xu, and L.-J. Lin, "Quasi-lumped design of UWB BPF using suspended stripline," *Progress In Electromagnetics Research Letters*, Vol. 11, 65–72, 2009.

14. Chen, M., C.-Y. Jiang, W.-Q. Xu, and M.-H. Ho, "Design of high order suspended stripline bandpass filter with miniaturization," *Progress In Electromagnetics Research Letters*, Vol. 8, 9–17, 2009.
15. Chen, M., M.-H. Ho, W.-Q. Xu, L.-J. Lin, and W.-H. Hsu, "Designs of suspended stripline filters using quasi-lumped elements approach," *Intl. Journal of Electrical Engineering*, Vol. 17, No. 3, 231–239, 2010.
16. Ouyang, X. and Q.-X. Chu, "A mixed cross-coupling microstrip filter with multiple transmission zeros," *Journal of Electromagnetic Waves and Applications*, Vol. 25, Nos. 11–12, 1515–1524, 2011.
17. Chu, Q.-X. and L. Fan, "A compact bandpass filter with source-load coupling by using short-circuited coupled lines between ports," *Journal of Electromagnetic Waves and Applications*, Vol. 24, Nos. 11–12, 14934–1500, 2010.
18. Weng, M. H., C. H. Kao, and Y. C. Chang, "A compact dual-band bandpass filter with high band selectivity using cross-coupled asymmetric SIRs for WLANs," *Journal of Electromagnetic Waves and Applications*, Vol. 24, Nos. 2–3, 161–168, 2010.
19. Fan, J.-W., C.-H. Liang, and X.-W. Dai, "Design of cross-coupled dual-band filter with equal-length split-ring resonators," *Progress In Electromagnetics Research*, Vol. 75, 285–293, 2007.
20. Xu, W.-Q., M.-H. Ho, and C.-I G. Hsu, "Quasi-lumped design of UMTS diplexer using combined CPW and microstrip," *Microwave and Optical Technology Lett.*, Vol. 51, No. 1, 150–152, 2009.
21. ADS, Agilent Technologies Inc., United State CA, 2011.
22. CST studio suite 2011, Computer Simulation Technology AG, Germany, 2011.
23. Kajfez, D., "Computed model field distribution for isolated dielectric resonators," *IEEE. Trans. Microwave Theory Tech.*, Vol. 32, No. 12, 1609–1616, 1984.
24. Hong, J. S. and M. J. Lancaster, *Microstrip Filters for RF/Microwave Applications*, Chapter 2, John Wiley & Sons, New York, 2001.